

CORRELATION BETWEEN PHOTODIODE MONITORING AND HIGH SPEED IMAGING OF THE DYNAMICS CAUSING LASER WELDING DEFECTS

Paper 1708

Peter Norman, Hans Engström, Per Gren, Alexander F. H. Kaplan

Department of Applied Physics and Mechanical Engineering,
Luleå University of Technology, SE-971 87 Luleå, Sweden

Abstract

Today merely a few monitoring systems for in-process detection of laser welding defects are commercially available. Despite a trend towards cameras, industrially more robust is still a photodiode, measuring in an optically filtered spectral window either the thermal emissions from the melt and vapour or the laser beam reflections. The monitoring rule for each application is identified empirically through correlations between the signal dynamics and welding defects, as the linking mechanism is non-trivial and therefore hardly understood. Thus the method does not provide a systematic guideline to detect a certain welding defect.

The here presented approach studies the context between the photodiode signal, the welding defects and the vapour, melt pool, keyhole and temperature dynamics. Simultaneous laser-illuminated high speed imaging is compared to photodiode monitoring at three spectral windows in order to identify through simultaneous timing any linking dynamics in a qualitative manner. Supportive methods are emission modelling and thermal imaging. Several cases of joints, materials and defects were studied to develop an illustrated theoretical description of the defect-signal correlations.

Introduction

Although laser welding has the potential for high quality, the operating window is often very narrow, thus different types of welding defects can easily occur. In-process monitoring of defects by photodiodes or cameras can reduce or eliminate expensive post-inspection. However, monitoring is based on empirical methods that cannot guarantee to monitor a correlation signal-defect.

Motivation of the present study is to explain the phenomenological links between a defect generation mechanism and the resulting monitoring signal in order to facilitate a judgement whether and how monitoring is possible for a certain defect. For this purpose, the combination of high speed imaging of the weld pool with modelling of the emissions from the weld pool to

a photodiode sensor shall enable to deeply explain and to predict the signal response on a certain defect.

As laser welding is a highly complex process comprised of several non-linear mechanisms, such as thermodynamic, fluid-mechanic and optical ones that interact with each other the complexity of modelling is very high. The keyhole and the movement of the melt relative to the laser beam can be modelled by using simplified approaches [1,2] that in many cases emanate from Rosenthal's theory of moving sources of heat [3] from 1946. The complexity increases even more when trying to model a defect arising in the weld. Until recently it was difficult to simulate the complex melt flow inside the weld pool but recently with massive computer power successful results were achieved, although various uncertainties remain.[4]

To visualise defect formation and fluid flow different tools have been developed, such as the X-ray transmission imaging system by Matsunawa and Katayama [5] that images the keyhole and melt-pool motion from the side. This setup is also useful for visualising pore formation. To visualise the top of the melt-pool it is possible to use high-speed imaging [6] or other [7] methods as the top surface is visible (by filtered laser-illuminated imaging) in contrast to volumetric mechanisms. The modelling of the melt pool surface and its motion is highly complex, therefore in the present approach we start from high-speed imaging as evidence to be able to model the correlation of the photodiode signal to the resulting surface.

As a first step [8] the melt pool and keyhole radiations to a sensor were modelled for hypothetical melt pool situations, namely melt pool temperature/boundary oscillations and keyhole opening oscillations. The model enabled a detailed analyse of the mechanisms and locations that are mainly responsible for the resulting signal, as the dominance of one mechanism was not obvious.

In the following this model is applied, combined with high speed imaging, to two specific defect cases monitored by a photodiode.

Experimental diagnostics method

By using a Redlake HS-X3 high-speed camera, synchronised together with a Precitec LWM monitoring system consisting of three photodiodes, we try to correlate defects in the weld and their dynamic observations to a signal from the photodiodes. The photodiodes have different characteristics; the plasma sensor P has a band pass filter for 400-600nm, the back reflection R is tuned to the laser wavelength 1064nm and the temperature sensor T is band passed between 1100nm and 1800nm. The weld pool is illuminated with a pulsed diode laser (500 W during 250 ns at 4 kHz) from Cavitator at 810nm wavelength and this light is detected by the high-speed camera through a narrow band pass filter at 810 +/-2nm.

The set-up, shown in Fig. 1, consist of: (1) the workpiece; (2) the focusing optics for the beam; (3) the pulsed laser illumination; (4) the high speed camera that is tilted 45 degrees to the side; and (5) the three photodiode sensors P,R,T placed coaxially. The area of the T-sensor studied in the present paper is a circle with a diameter of 5 mm, corresponding to a projected 10 mm circle diameter at the surface, concentric to the laser beam. The data from the photodiode sensors are recorded at 8 kHz and from the camera at 4 kHz.

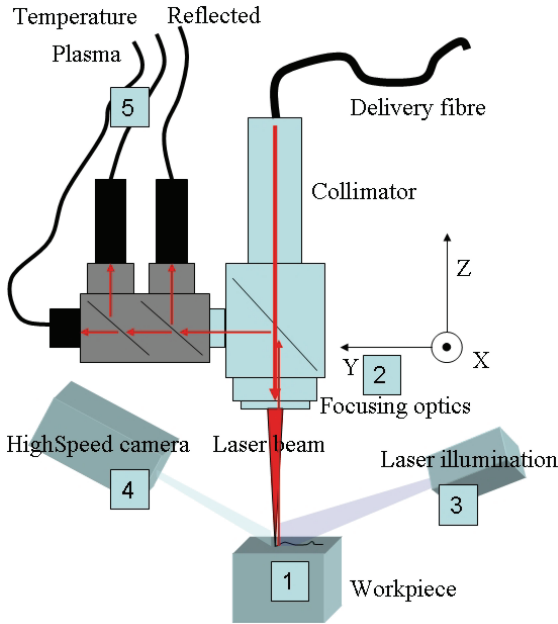


Figure 1: Experimental set-up for the diagnostics of laser welding

Mathematical emission model

In principle, the photodiode signal results from the sum of those photons in the corresponding spectral range

(P,R,T-sensors) that travel from the processing zone to the sensor, as a function of time, see Fig. 2(a). In detail, each surface element i of defined discretisation area A contributes to the signal, see Fig. 2(b), according to its geometrical orientation θ relative to the sensor, including the angular radiation characteristics $\cos^2(\theta)$, along with its temperature T dependent emitted power density q and its emissivity ε .

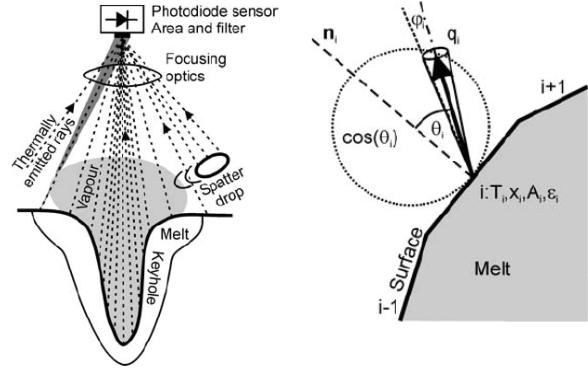


Figure 2: (a) Thermal emissions from the weld pool surface, incl. keyhole, vapour plume and spatter, to a photodiode sensor. (b) thermal radiation flux q_i from an inclined liquid surface element i to the sensor

The above is valid for the T-sensor, but additional contributions from the metal vapour plume can contribute to the sensor. For the P-sensor the principle is the same, but the shorter wavelength filter favours photons from the hotter metal vapour to photons from the surface. The R-sensor accumulates reflected laser beam photons according to geometry and absorptance.

The research approach applied in the present study starts from high speed images as experimental evidence of the geometry of the melt pool and keyhole as a function of time that can be quantitatively evaluated. From the dimensions the surface temperature field $T(x;t)$ is approximated. Integrating for each time step over the relevant surface area, a mathematical model is developed according to the above described mechanisms, that calculates the accumulated power of thermal emissions hitting the T-sensor. The research hypothesis is that this calculated signal corresponds to the sensor signal, thus the mathematical model enables deep analysis. The emissivity of the surface has to be estimated, radiation from the metal vapour is assumed to be neglected for the sake of simplicity. We postulate the research hypothesis that the T-sensor signal is mainly governed by the geometrical conditions at the weld pool surface, which can be identified by high speed imaging.

Thus, prescribing a certain dynamic situation of the weld, the emitted radiation incident on the sensor and the resulting voltage signal can be modelled, as follows. Thermal radiation from the surface contributes to the signal, which can be considered by ray tracing of all surface elements visible by the sensor. Figure 2(b) illustrates that the summation of all radiation does not simply correspond to the projected surface visible by the sensor. Instead, surface domains with steeper angles (e.g. the keyhole) contribute larger according to their larger area, as was also experienced during thermal (IR) imaging. Spatter drops shadow part of the emitting pool surface, but instead radiate by themselves, see Fig. 2(a). The rays travel through the metal vapour cloud and shielding gas as well as through the focusing optics.

The sensor has a certain size and is thus hit by a small cone/pyramid (of angle φ) bunch of rays rather than a single ray of light, see Fig. 2, described by a view factor C_v . Surfaces have a certain angle-dependent radiation characteristics with the power density depending on the angle to the normal by $\cos^2(\theta)$. Moreover, the power density of radiation propagating in the cone decreases at distance R by $1/R^2$ corresponding to an expanding spherical surface area.

For a certain surface element i , Figure 2(b) also illustrates that the power P_i from each ray/cone, Eq. (1), depends on the surface element area A_i , on the temperature T_i and on the emissivity ε_i . The power density q_{tot} is calculated by the Planck's radiation law, Eq. (3), in terms of power density per spectra λ [$\text{W}/\text{m}^2 \cdot \text{m}^3$].

This can be summarised in the following equations:

$$P_i = A_i \cos^2(\theta_i) C_{vi} q_{tot} \quad (1)$$

where C_{vi} is the view factor [8]

$$C_v = \frac{A_s}{2R_s^2 \pi} \quad (2)$$

$$dq(\lambda; T) = \frac{4\pi hc}{\lambda^5} \frac{1}{e^{hc/\lambda k_B T} - 1} d\lambda \quad (3)$$

(wavelength λ , Planck's constant h , vacuum speed of light c , Boltzmann's constant k_B)

To estimate the temperature field by matching the melt pool and keyhole surface shape obtained from

imaging, we first tried the model [9] of superimposed moving point sources of heat, Eq. (4).

$$T(x, y, z) = T_a + \frac{P}{2\pi k r} e^{(-Pe'(x+r))} \quad (4)$$

that has the radial distance r in Cartesian coordinates

$$r = \sqrt{x^2 + y^2 + z^2} \quad (5)$$

and the (relative) Péclet number with v as the weld speed (in x -direction) and κ as the thermal diffusivity:

$$Pe' = \frac{v}{2\kappa} \quad (6)$$

However, despite using the point source power as a matching factor, the obtained melt and vapour surface isotherms differed too much from the shapes obtained from high speed imaging, that were in practice approximated by ellipses with the essential coordinates as shown in Fig. 3(a), dividing the surface into four domains: keyhole KH, unoxidised liquid L, oxidised weld pool OX, solid S.

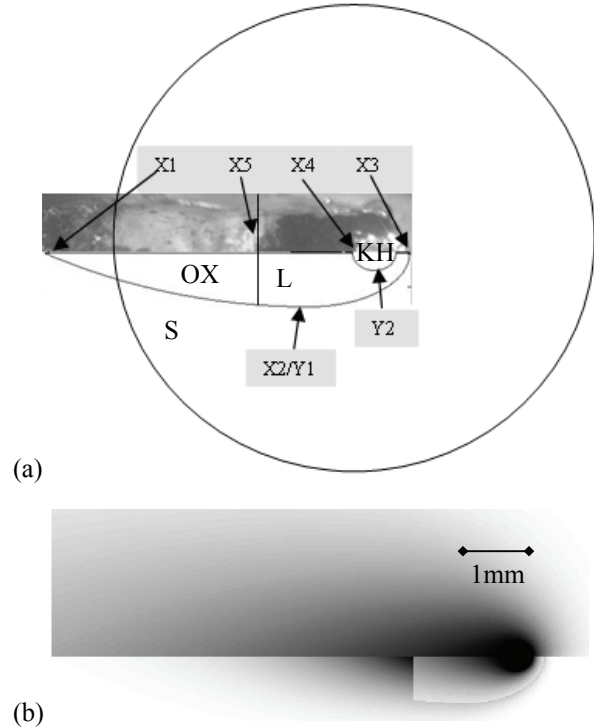


Figure 3: (a) Geometrical definition of the four emitting domains, identified from a high speed image and circular (10 mm) sensor area at the workpiece surface; (b) example (humping case below, $t = 0.182$ s)

of a modelled surface temperature field (upper), calculated power density hitting the sensor (lower half)

Thus instead the temperature field was modelled by applying an exponential function (from the beam axis), matching for each radius the measured keyhole (evaporation isotherm) $T_v(r_v(\phi))$ and the melt pool (melting isotherm) $T_m(r_m(\phi))$, by solving the two constants $C_1(\phi)$, $C_2(\phi)$:

$$T(\phi) = T_a + C_1 \exp(-C_2 r) \quad (7)$$

Figure 3(a) shows an example image from the humping case studied below where the rear part of the melt surface was oxidised (Cr_2O_3 , remaining solid), thus requiring the solid emissivity for the model. Therefore the location of the oxidised melt is considered, too. The circle of the projected sensor area is also shown in Fig. 3(a) as the area to be integrated. One important aspect is that part of long melt pools can be out of the sensor area, thus being not detected.

In this work we only look at the radiation between 1100 nm and 1800 nm (sensitive range of the temperature sensor T) so we will calculate the power emitted over a certain wavelength range $\Delta\lambda$ from the elements of area A at the temperature T of each element, see Fig. 2(b). A simplified formula can be used, being a numeric approximation over the chosen wavelength range.

$$\Delta P = \frac{2\pi h c^2}{\lambda^5} \frac{1}{e^{hc/\lambda k_B T}} \Delta\lambda A \varepsilon \quad (8)$$

This value is then used to calculate the amount of energy hitting the T-photodiode. As the sensor is placed concentric to the melt pool and no severe geometrical inclinations contribute to the radiation, both the view factor and the $\cos^2(\theta)$ dependence do not need to be taken into account in the present study (but can be easily introduced in future analysis). A constant value was used (from literature) for the emissivity of the solid (same for the solid oxide layer on the liquid) and for the liquid, here $\varepsilon_s = \varepsilon_{ox} = 0.4$ and $\varepsilon_l = \varepsilon_{kh} = 0.2$, as the liquid is highly reflective. $\varepsilon_l = 0.3$ could be more accurate,[10] but with $\varepsilon_l = 0.2$ the influence of different emissivities becomes clearer. Further investigations on identifying the emissivity will be conducted soon.

For the example shown in Fig. 3(a), the modelled temperature field is shown in Fig. 3(b), upper half, while the modelled power density field of radiation hitting the T-sensor is shown in Fig. 3(b), lower half. It can be clearly seen that contributions from the solid

and oxide can become essential, due to higher emissivity. Otherwise the T^4 -nature (approximately, Stefan-Boltzmann law) of thermal emissions clearly shows the overproportional areas of contribution decaying faster than the temperature field. Radiation from the metal vapour jet is neglected. For radiation from the keyhole, the keyhole is approximated by a cone. The cone has an inclination angle α

$$d \tan(\alpha) = r_{kh} \quad (9)$$

according to the keyhole radius r_{kh} corresponding to the (averaged) dimensions identified by high speed imaging and the welding depth d (note: blind weld), equally emitting power from each keyhole wall surface element

$$P_{i,kh} = \varepsilon_l q(T_v) \cos^2\left(\frac{\pi}{2} - \alpha\right) \frac{A_i}{\tan(\alpha)} = \varepsilon_l P(T_v) \frac{1}{2} \sin(2\alpha)$$

Eventually the (non-calibrated) power on the sensor (or signal) calculated is composed of the separate integration over the four domains, see Fig. 3(a):

$$P_s = P_{kh} + P_l + P_{ox} + P_s \quad (10)$$

Various joint cases were studied. Two of them are here presented, namely (i) monitoring of the criterion of sufficient weld width in overlap configuration for different welding speed and (ii) monitoring of humping drops. Stainless steel AISI 304 was welded as an overlap joint (zero gap), a 1 mm sheet on a 4 mm sheet (100 mm x 50 mm). A 3 kW cw-Nd:YAG laser beam (0.6 mm fibre) was focused to a 600 μm spot (located on the surface). Ar was applied from a side nozzle as shielding gas.

Results Case I: Weld width for various speed

The optimum weld was defined to primary have a weld width wider than the thinner sheet thickness (1 mm), secondary maximum welding speed. The welding speed was varied from 1 to 6 m/min in 1 m/min-steps.

Photos of the top surface appearance of the resulting welds were taken, see Fig. 4(a), showing a regular, smooth weld. Micrographs of the weld cross section were made, see Fig. 4(b) and evaluated with respect to the weld dimensions, see Fig. 4(c). For a speed of 4, 5 and 6 m/min the upper 1 mm-plate was not welded through. For a speed of 2 and 3 m/min it was welded through, but the weld had a lower width than the criterion (>1 mm). Only for 1 m/min the weld was acceptable, which is impossible to judge from the top surface width. The weld width both at the top and at the interface decreases gradually with speed (as can be expected).

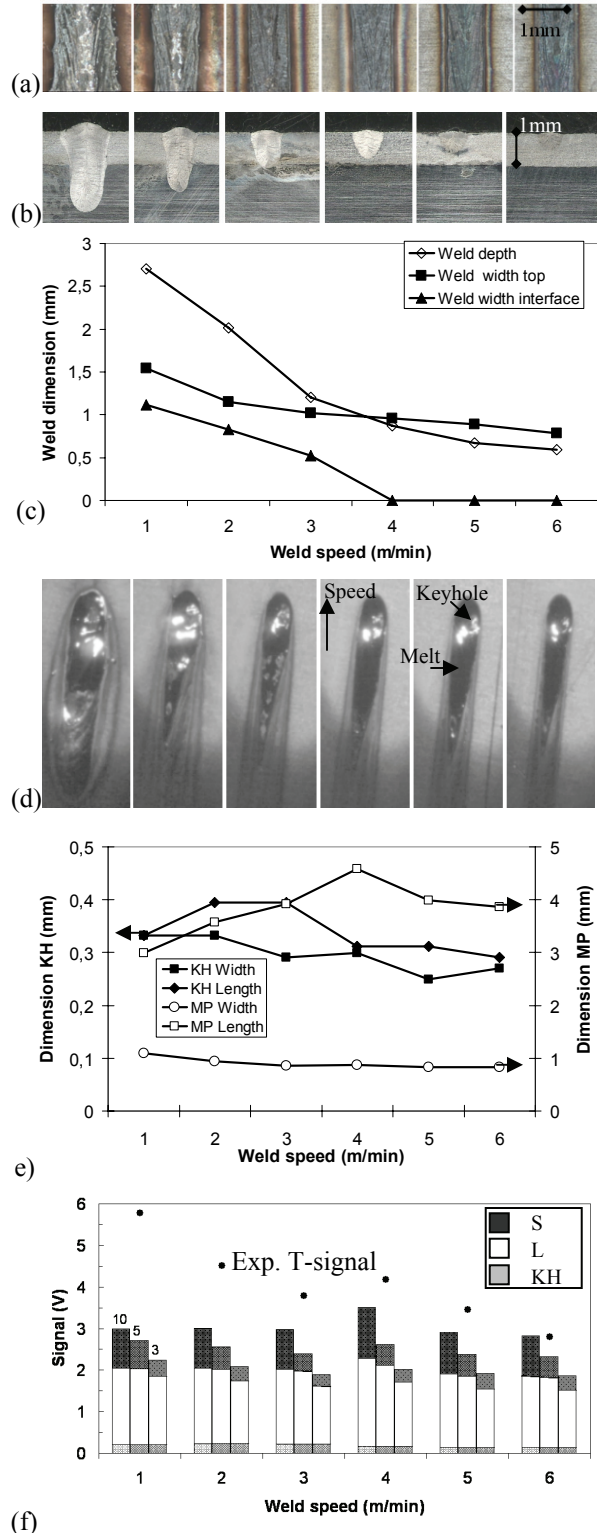


Figure 4: Evaluation vs. speed 1 – 6 m/min (from left)
 (a) weld top appearance
 (b) weld cross section micrograph
 (c) weld cross section dimensions vs. speed
 (d) keyhole and melt pool HS images;

(e) imaging melt pool (MP), keyhole (KH) dimensions
 (f) average experimental T-signal; calculated signal, composed of the three contributions KH,L,S for three sensor projection diameters (10, 5, 3 mm)

The process was recorded by high speed imaging for each speed, shown in Fig. 4(d). Note that the images are 45° inclined as viewed from the side, which was corrected during the evaluation. The process was very stable and calm for all speeds, thus the shown images are highly representative.

The evaluation of the melt pool and keyhole dimensions from imaging according to the definitions in Fig. 3(a) is shown in Fig. 4(e). The keyhole is widely circular, slightly decreasing in size with increasing speed. It is interesting to note that the weld pool width initially increases for increasing speed but beyond a maximum (here: 3 m/min) decays. Such behaviour is difficult to explain solely from thermodynamics. One hypothesis is that the absorption conditions (Brewster angle, multiple reflections, beam trapping) according to the keyhole shape are optimum at this speed.

The average value of the T-photodiode signal shown in Fig. 4(f) for the different speeds seems to follow a combination of both trends, namely basically a decrease with increasing speed, according to the decrease of the weld width, but also having a distinct maximum at 3 m/min. Note that also the R-signal was recorded but not evaluated yet.

From geometrical dimensions of the weld pool for the six speed cases, Fig. 4(c), the above presented mathematical model was applied. The calculated power per welding speed is shown in Fig. 4(f).

Beside the sensor dimension of a 10 mm diameter circle (projection at the surface), also the dimensions of 5 mm and 3 mm were studied, also shown in Fig. 4(f), as there were indications that the size or location is uncertain, but essential. As the outer solid regions contribute with less than 0.1% to the power on the sensor, smaller sensor areas cutting off a larger part of the melt would also be equivalent to a misalignment of the sensor. These results are of interest, as the results for 5 mm and particularly 3 mm excellently match the signal trend, while the 10 mm sensor results miss the peak at low speed. The cut-off could be an explanation.

It can be analysed that the melt contribution is the dominant one to the sensor, thus a mix of high temperature but also large area, while the contribution by the keyhole is the smallest one. the trend of less

signal value for higher speed corresponds to the weld width both at the top and in the interface, which is approximately reflected by the contributions from the solid and liquid. However, the long, large weld for 4 m/min makes an exception in the sensor signal and HS-images, but not in the weld width, thus making reliable monitoring difficult in this case. As mentioned before, if part of the melt is out of the range of the sensor area, it can affect the signal essentially.

Fig. 5 shows for a speed of 2 m/min as example how the signal and its smoothed version looks like along the straight weld. Note that for certain speeds the constant period was shorter, instead a gradual signal increase was observed.

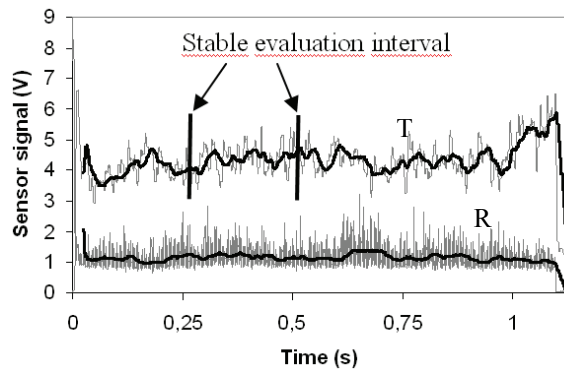


Figure 5: Acquired and smoothed T- and R-photodiode sensor signal during a complete weld at 2 m/min; interval for deriving the average value

The above findings of Case I are illustrated in Fig. 6 by the Bifurcation Flow Chart method, BFC, recently developed by the authors.[11] The basic idea is to illustrate the essential mechanisms observed (by imaging) for the occurrence of a certain defect, compared to a good weld. Only the essential mechanisms shall be considered and only the observed facts or highly probable mechanisms, in a manner as fundamental as possible. The method basically enables generalisation when compared with other findings with partially same chart objects.

Briefly, the BFC for Case 1 explains that the criterion is simply whether the whole desired width w_{min} at the thickness d_i of the upper sheet exceeds the melting temperature, T_m . The essential mechanisms responsible are the lateral heat flow and the width of the formed keyhole, both in turn depending on energy parameters like power, speed and focal spot diameter. While the images are observed facts Γ , the BFC can be resolved further in the future by explaining the responsible mechanisms and their links to the parameters.

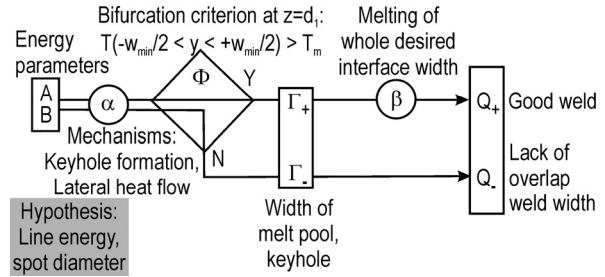


Figure 6: Illustrative theoretical description of Case I by a BFC

Results Case II: Periodic humping drops

The other case studied consists of the same set-up as previously but for this case regular humping drops formed during welding, as can be clearly seen from the weld surface appearance in Fig. 7. The acquired T-signal and its local average value is shown, too.

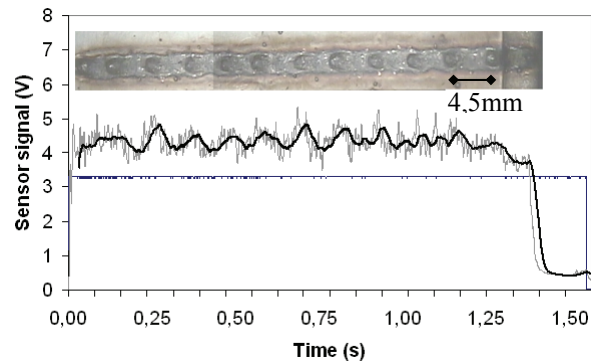


Figure 7: Acquired and smoothed T-photodiode signal of a complete weld; top surface appearance photo with humps

Note that the same parameters were tried as above, here for the speed of 2 m/min (and 3 kW beam power), but the result was not reproducible as now humping took place, which did not happen before, obviously due to slight changes in the shielding gas. This shows how sensible a process can react on slight changes and that high control of all parameters is important. Nevertheless, independent of the cause, for the present study the presence of humping was very interesting as the humping periodicity is clearly visible in the signal, particularly in the filtered, thus smoothed version, see Fig. 7. The first signal peaks and valleys correspond exactly to one hump, while against the end of the weld the signal shows some additional maxima (smaller peaks before that have grown).

In Fig. 8(a) a magnified interval of almost two humping periods of the signal (and its averaged

version) is shown (for the third hump of the weld). The eleven arrows indicate corresponding HS images, shown in Fig. 8(c), that was selected for analysis and modelling of the process and signal. Again the defined dimensions according to Fig. 3(a) were measured from the images, see Fig. 8(b), now as a function of time and including the oxide layer location due to its significant presence in this case (being an indicator for different shielding gas conditions). Note that the connection between the measured points is just an indicator and does not necessarily represent the behaviour in between.

The reason why most of the selected time steps was chosen such that it gathers around two periods rather than being equidistant becomes clear from Fig. 8(b): From observing the imaging clips it was obvious (for all humping events) that a relatively quick shortening of the weld pool took place periodically, accompanied with an even faster propagation of the oxide layer that then slowly retreats. In order to consider this fast event in the study, several instants around this event were selected, as it can be essential for the emission characteristics. Note also that the smoothed signal falls faster than it rises.

It is evident that each hump period is noisy, although it is possible to say that when the oxide is forming, a clear decrease in the smoothed signal can be seen. When the hump is fully developed and the oxide layer has retreated, the signal is at the top.

In Fig. 8(d) the calculated emitted power density is plotted, showing clearly the different radiation patterns from the liquid, solidus and keyhole. The sharp edge below the keyhole indicates the solid Cr_2O_3 -oxide layer on the liquid that is simulated with the same emissivity ϵ_s as the solidus.

In Fig. 8(e) the modelled results for the radiation power contributions from the keyhole, blank melt, oxidised melt and solidus are plotted as a function of (for the selected time steps) against the experimental sensor signal. Note that here only a comparison with the direct sensor signal makes sense, while the averaged value just shows trends but would give a wrong value. Again the contribution from the keyhole is little, the blank liquid is the dominant part, but also the oxidised pool has a significant contribution, particularly a strong dynamics.

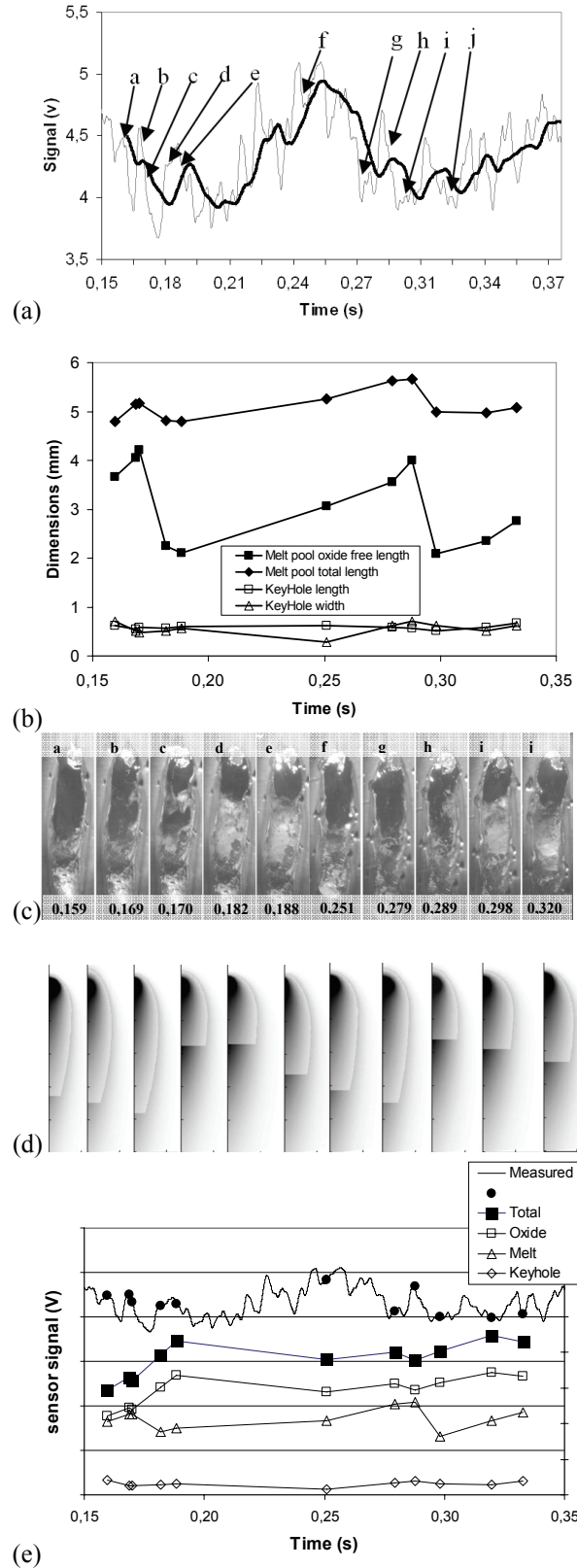


Figure 8: Evaluation of 1.5 hump cycles (11 instants): (a) acquired and smoothed T-photodiode signal during approx. 2 periods.

- (b) melt pool, oxide and keyhole dimensions
- (c) HS images of keyhole, melt pool and oxide
- (d) calculated power density emitted from the surface
- (e) experimental and calculated T-sensor signal composed of the four contributions KH,L,OX,S

The fact of the same basic periodicity (in average all 117 ms, i.e. 8.57 Hz) of four mechanisms, namely the humps, the signal, the melt pool length (thus probably also the temperature field) and the oxide layer extent is a clear evidence of a strong interdependence between them. Further peaks in the signal indicate additional events being an order of magnitude faster.

Nevertheless in this case direct correlations between the calculated and the experimental signal are not obvious. The signal has its valley where just when the oxide layer is short and starts its rapid growth (and vice versa for the blank liquid surface), but the present model could not predict this trend, rather vice versa.

One hypothesis is that the temperature field cannot be directly derived from the isotherms but has a phase shift, as oscillating. Moreover, the emissivity and the temperature of the oxide bear uncertainties. In contrast to a calm weld with a smooth surface as in the first case, the humping drop and also the accompanying melt dynamics around the keyhole has surface elevations that were neglected in this first study but could be considered as angle-dependent contributions.

Additional analysis of the images and perhaps refined modelling is required. In the future the high speed imaging of the melt surface will also be accompanied by thermal imaging and by (non-filtered) imaging of the metal vapour jet.

Same as for Case I, a BFC for Case II was developed, shown in Fig. 9, for providing a theoretical description of the findings. Briefly summarised, the condition whether a humping defect is formed or not was observed to originate from a melt flow upwards in a temperature environment with latent resolidification behaviour. Once the resolidification of the hump starts, further melt flows upwards and resolidifies, growing the hump. Evident phenomena observed from imaging were several accompanying periodic events β shown in the BFC. The early mechanisms α leading to the hump bifurcation are generally speaking the intensities of the motions in the system keyhole-melt pool. Their dependence on the parameters is indirect and not obvious until further resolution of the BFC-uncertainties.

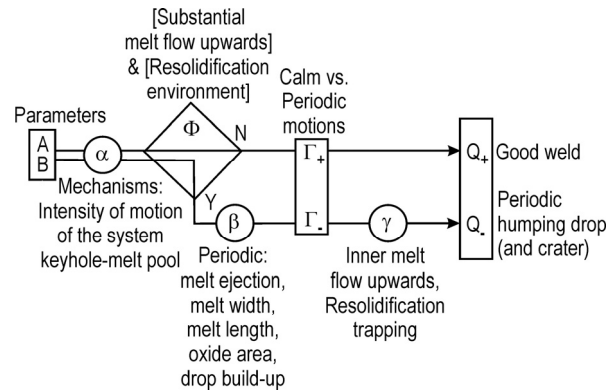


Figure 9: Illustrative theoretical description of Case II by a BFC

Conclusions

Analysis of the signal of photodiode based monitoring of laser welding can be highly valuable for judging the potential and limits of monitoring applications.

The method developed turns out to be powerful, i.e. accompanying high speed imaging and its quantitative evaluation as the boundary conditions for an emission model that aims to predict the monitoring signal. Both, the images and the model enable deep analysis, as was demonstrated for a steady state case at different speeds and a time-dependent humping case

For the cases studied it can be concluded:

- The signal is mainly governed by the liquid pool emissions, thus in turn by the temperature field and the pool size
- Oxidation of the weld pool surface can significantly change the emissivity and thus the signal
- For the steady state case, imaging along with modelling could clearly explain why the dominating signal trend can be broken, as here for a suddenly longer weld pool
- If part of the melt pool is outside the detectable domain, this can strongly affect the signal; thus the detection area is important
- For the oscillating humping case, imaging gave clear evidence on interdependencies between certain mechanisms, but the model at this stage could not give an explanation

References

- [1] Lampa, C., Kaplan, A.F.H., Powell, J., Magnusson, C., (1997), An analytical thermodynamic model of laser welding, *J. Phys. D: Appl. Phys.* 30, pp. 1293-1299
- [2] Al-Kazzaza, H., Medraja, M., Caob X., Jahazib M., (2008), Nd:YAG laser welding of aerospace grade ZE41A magnesium alloy: Modelling and experimental investigations, *Materials Chemistry and Physics* 109, pp. 61-76.
- [3] Rosenthal, D., (1946), The theory of moving sources of heat and its application to metal treatments, *Trans. ASME*, 48, pp. 848-866.
- [4] Otto, A., M. Geiger, (2007), From basic research to industrial applications – new developments for laser welding, *Proc. LIM 4*, June 2007, Munich (D), WLT, p 5-11.
- [5] Katayama, S., Matsunawa, A., (2001), Microfocused X-ray transmission real-time observation of laser welding phenomena, *Yosetsu Gakkai Shi/Journal of the Japan Welding Society*, v 70, n 6, September, 2001, pp. 17-22
- [6] Norman, P., Engström, H., Kaplan, A.F.H., (2007), State-of-the-art of Monitoring and Imaging of Laser Welding Defects. *Proc. 11th Nordic Laser Material Processing Conference, NOLAMP 11*, Aug. 20-22, Lappeenranta Univ. of Technology; Lappeenranta.
- [7] J. Shao, Y. Yan, (2005), Review of techniques for on-line monitoring and inspection of laser welding, *Journal of Physics: Conference Series*, v 15, n 1, p 101-7.
- [8] Norman, P., H. Engström, A. F. H. Kaplan, (2007), Modelling of the impact of melt surface dynamics on a photodiode monitoring signal in laser welding, *Proc. ICALEO*, Oct 29-Nov 2, Orlando (FL), Laser Institute of America.
- [9] Resch, M., Kaplan, A.F.H., (1998), Heat conduction modelling of laser welding, *Lasers in Engineering*, Vol 7, pp. 229-240
- [10] Del Campo, L., Pérez-Sáez, R. B., Esquisabel, X., Fernández, I., Tello, M. J., (2006), New experimental device for infrared spectral directional emissivity measurements in a controlled environment, *Review of Scientific Instruments*, Volume 77, Issue 11, pp. 113111-113111-8.

[11] Kaplan, A. F. H., Norman, P., Gren, P. and Powell, J., (2008), The role of uncertainty in the theoretical description of laser welding, submitted.

Acknowledgements

This work was funded by VINNOVA, The Swedish Innovation Agency, projects no. 2006-00668, 2005-02895, 2006-00563, and by the Kempe foundation. The authors are also grateful to Precitec GmbH for their support.

Meet the Authors

Peter Norman was born in Luleå in the north of Sweden in 1974. He studied mechanical engineering at Luleå University of Technology, got a Bachelors degree in 1997 and graduated at the Master level in 2002. He worked at a steel mill as researcher for two years, and after that returned to the university as PhD-student, receiving the Technical Licentiate degree on process monitoring of milling in 2006.

Hans Engström was born in Luleå, Sweden in 1951. He carries out research in different areas of laser materials processing at Luleå TU for more than 25 years, e.g. for his Licentiate thesis on laser cladding. Moreover, he is deputy head of division and he teaches LEAN manufacturing to Swedish industry.

Per Gren was born in Sweden in 1958. He is employed as senior lecturer at the Division of Experimental Mechanics, Luleå University of Technology, Sweden. His research comprises the development and application of optical methods for the study of mechanical, acoustical and thermal properties.

Alexander Kaplan was born in Vienna, Austria in 1967, employed as researcher at Vienna TU from 1989 until 2000, receiving a PhD-degree in 1994. After a post-doc year at Osaka University, Japan, from 2002 on he has been appointed as professor and head of division on manufacturing at Luleå University of Technology, Sweden. His research focus comprises laser materials processing, in particular process modelling, laser welding and hybrid welding.